REVIEW ARTICLE   OPEN

Check for updates

Majorana modes with side features in magnet-superconductor hybrid systems

Daniel Crawford [1], Eric Mascot [1,2], Makoto Shimizu [3], Philip Beck [4], Jens Wiebe [4], Roland Wiesendanger[4], Harald O. Jeschke [5], Dirk K. Morr [2] and Stephan Rachel [1]✉

Magnet-superconductor hybrid (MSH) systems represent promising platforms to host Majorana zero modes (MZMs), the elemental building blocks for fault-tolerant quantum computers. Theoretical description of such MSH structures is mostly based on simplified models, not accounting for the complexity of real materials. Here, based on density functional theory, we derive a superconducting 80-band model to study an MSH system consisting of a magnetic manganese chain on the s wave superconductor niobium. For a wide range of values of the superconducting order parameter, the system is a topological superconductor, with MZMs exhibiting non-universal spatial patterns and a drastic accumulation of spectral weight on both sides along the magnetic chain. These side feature states can be explained by an effective model which is guided by the ab initio results. Performing scanning tunneling spectroscopy experiments on the same system, we observe a spatial structure in the low-energy local density of states that is consistent with the theoretical findings. Our results open a first-principle approach to the discovery of topological superconductors.

npj Quantum Materials (2022)7:117 ; https://doi.org/10.1038/s41535-022-00530-x

INTRODUCTION

Topological superconductors are amongst the most desirable materials, as their quasiparticles at zero energy, known as Majorana zero modes (MZMs)[1–4], exhibit non-Abelian braiding statistics[5]. These MZMs are promising candidates for topological qubits[6] and for next-generation quantum computing devices. Magnet-superconductor hybrid (MSH) systems[7–12] offer a particularly appealing platform: (i) they are comprised of well-understood components, magnetic atoms such as Mn, Fe, or Co deposited on the surface of a conventional superconductor such as Nb, Re or Pb; (ii) by virtue of single-atom manipulation techniques the magnetic structures can be assembled on the atomic level; (iii) scanning tunneling methods allow the local measurement and manipulation of such structures. Despite the tremendous progress, both experimentally and theoretically, in the past years, one-dimensional MSH structures[13–20], i.e., magnetic chains on the surface of superconductors with spin–orbit coupling due to the inversion-symmetry breaking at that surface, still struggle with either sample quality or the size of the spectral gap necessary to separate the MZMs from the low-lying excited states. On the theoretical side, most simulations are (i) based on simplified models[7,9,21–23] and (ii) often done for entirely one-dimensional structures[7,21], thus ignoring the complexity and the two- or three-dimensional character of the materials involved. In addition, such models often couple both the magnetic Zeeman field (accounting for the magnetic moments) and the superconducting order parameter (accounting for the superconducting proximity effect) to the same orbitals, which is unphysical. Despite these simplifications, such models clearly show topological phases with localized MZMs at chain ends. Early experiments for Fe chains on Pb(110)[13] seemed to be in good agreement with such modeling. Subsequent experiments on Fe/Pb(110) revealed a peculiar *double eye* feature[24], which was explained by the authors of ref. [24] through

the interplay of a local suppression of the order parameter in the vicinity of the magnetic chain and the tunneling geometry, including the tip trajectory. However, the aforementioned simplified models in the literature cannot capture features such as the double eye. In the experimental part of this paper, we present d*I*/d*V* scanning tunneling spectroscopy data for Mn/Nb(110) and Fe/Nb(110) systems where characteristic low-energy states are present on the sides of the magnetic chain. We perform ab initio modeling of Mn chains along [001] on Nb(110). We construct an effective superconducting 80-band Bogoliubov-de Gennes model, which turns out to be topologically non-trivial for most of the considered parameter range of the superconducting order parameter. Analysis of this model guides us to construct a further simplified model–still containing a four-atomic unit cell and a non-trivial amount of hoppings beyond nearest-neighbors-where the zero-energy states for the topological phase exhibit side-features. Further investigation of this model reveals that the spatial structure of the emerging MZMs sensitively depends on the size of the spectral gap, with low-energy features varying between localized along the side of the magnetic chains and localized near the end, with the latter resembling the previously observed double-eye feature. Due to the promising agreement of the modeling with our scanning tunneling experiments for Mn chains on Nb(110) and the similarities to other MSH structures, such as Fe chains on Nb(110) or Pb(110), our work questions the notion of point-like MZMs as the hallmark of one-dimensional topological super-conductors. We furthermore propose that MZMs appearing as side features might be a common property of topologically non-trivial MSH structures in the small gap regime due to the complex interplay of the MZM's orbital composition and their repulsion from the magnetic chain.

[1]School of Physics, University of Melbourne, Parkville, VIC 3010, Australia. [2]Department of Physics, University of Illinois at Chicago, Chicago, IL 60607, USA. [3]Department of Physics, Okayama University, Okayama 700-8530, Japan. [4]Department of Physics, University of Hamburg, D-20355 Hamburg, Germany. [5]Research Institute for Interdisciplinary Science, Okayama University, Okayama 700-8530, Japan. ✉email: stephan.rachel@unimelb.edu.au
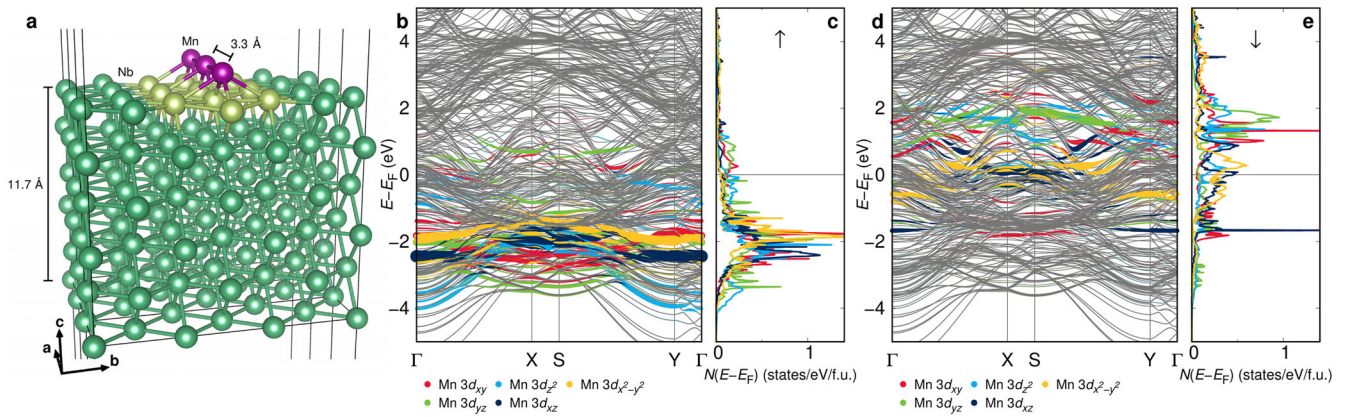
Fig. 1 Ab initio treatment of a Mn chain on the (110) surface of Nb. a Three unit cells used for the DFT calculations are shown; each unit cell contains 36 Nb and one Mn atom. The unit cell is oriented such that $a \parallel x$, $b \parallel y$ and $c \parallel z$, and on the Nb surface, $a \parallel [001]$, $b \parallel [1\bar{1}0]$. **b, d** DFT band structure for spin up and down, respectively, where the orbital character of the Mn d-orbitals is highlighted in color while all other orbitals are shown in gray. **c, e** Density of states (DOS) for the Mn d-orbitals from (**b, d**). Comparison of **c** and **e** clearly reveals the spin polarization.

RESULTS

DFT modeling

Using density functional theory (DFT) and projective Wannier functions, we study the electronic structure of Mn chains on Nb(110), and map it onto a tight-binding model to extract the orbital dependence, spin splitting, and spin–orbit coupling. To this end, we construct a slab supercell for the Mn chains along the [001] direction with $d_{\mathrm{Mn-Mn}} = 3.30$ Å on Nb(110). There is little previous work on ab initio-based modeling of MSH structures, see refs. [25,26] for two notable exceptions. Figure 1a shows the largest supercell that we can study computationally. The distortions of the relaxed Nb surface with Mn in the optimal hollow position (see Supplementary Note 1; Materials and methods are available as supplementary materials at the npj Quantum Materials website) entail that the Nb(110) electronic structure with a Mn chain attached differs from the bulk band structure both because of surface relaxation and because of distortions due to the Mn chain. Figure 1b, d shows the fully relativistic (GGA+SO) spin-polarized band structure of our system, with Mn orbital character highlighted. We find that the ferromagnetic arrangement is 29.4 meV/ Mn lower in energy than the antiferromagnetic one, indicating that Fig. 1b, d represents the DFT electronic ground state of the system. We find that an out-of-plane alignment of the magnetic moments is slightly lower in energy (by about 0.1 meV/Mn) compared to an in-plane alignment. To construct a tight-binding model of the bandstructure obtained from the DFT calculations, we use projective Wannier functions within FPLO[27]. However, the inclusion of all relevant orbitals, the Mn $3d$, $4s$, and $4p$, as well as all Nb $4d$, $5s$, and $5d$ orbitals, would result in a 666 band tight-binding model, whose investigation, for example, in terms of the topological invariant or its real-space properties, is computationally beyond our current abilities. To arrive at a tractable tight-binding model, we therefore restrict our attention to the Mn $3d$ orbitals and the Nb $4d$ orbitals that bond with them (see highlighted Nb sites in Fig. 1a). This results in a 40-band tight binding model, which (i) correctly reproduces the spectral weight of the Mn $3d$ bands (as given by the DFT results Fig. 1c, e), which are relevant for the emergence of topological superconductivity due to their magnetic moments, and (ii) contains the direction-dependent d orbital overlaps as well as the effects of Mn spin splitting and Nb spin–orbit coupling.

80-band model

We convert the DFT-based 40-band tight-binding model into a superconducting 80-band Bogoliubov–de Gennes model with the bare superconducting order parameter Δ as the only free parameter (see Supplementary Note 2). Note that we apply the superconducting onsite pairing term only to the orbitals of the three Nb atoms but not to the Mn atom; we assume that superconductivity is proximitized into the Mn orbitals, thus accurately describing the experimental system. It is important to emphasize that Δ here only serves as a phenomenological parameter and does not have a one-to-one correspondence with the superconducting gap (which is known to be $\Delta_{\mathrm{Nb}}=1.51$ meV for Nb). In fact, it is quite clear that the bare Δ must be chosen to be much larger since the three Nb atoms represent the super-conducting proximity effect of the entire (three-dimensional) Nb substrate. In order to investigate the topological phase diagram of this model we compute the gap size and the topological invariant $\mathcal{M}$[1] characteristic of topological class D[28,29]. The system is gapped, but the spectral gap is tiny for $\Delta < 130$ meV (Fig. 2a) and ranges between 7 and 188 µeV for periodic boundary conditions (mean value 69 µeV). Moreover, we find for $0 < \Delta < 120$ meV and for $\Delta > 130$ meV the ground state to be topologically non-trivial, i.e., $\mathcal{M} = -1$ (Fig. 2a). Gap sizes for the regime $\Delta > 130$ meV are in the range from 33 µeV to 1.83 meV (mean value 1.19 meV). Only the narrow region 120 meV $< \Delta < 130$ meV turns out to be trivial. Our momentum space analysis thus reveals that Mn chains in the [001] direction on Nb(110) realize a topological superconductor, which due to bulk-boundary correspondence is accompanied by MZMs that are localized at the chain ends. Chain length and effective gap size might, however, influence MZMs and cause them to hybridize in an oscillatory fashion as a function of length, which is one of the key signatures of hybridized MZMs in short chains[30,31].

Next, we study the real-space electronic structure, and in particular, that of the MZMs of the DFT-based 80-band model. For short chains, it is very difficult to find localized zero-energy states due to the tiny gap size leading to a severe hybridization of MZMs (Fig. 2b). Figure 2b reveals that there is no unique structure of MZMs, making it difficult to identify topological phases solely based on the spatial structure of the zero-energy local density of states (LDOS). However, our computation of the topological invariant in real space[32] shows that, as long as chains exceed ~10 sites, we find perfect agreement with our momentum space analysis shown in Fig. 2a. For $\Delta > 200$ meV we find examples of zero-energy LDOS where the hybridization leads to an oscillatory pattern and, quite astonishingly, the spectral weight of the MZMs is not located in the center of the chain but instead on the Nb atoms on the side of the magnetic chain. These side features show
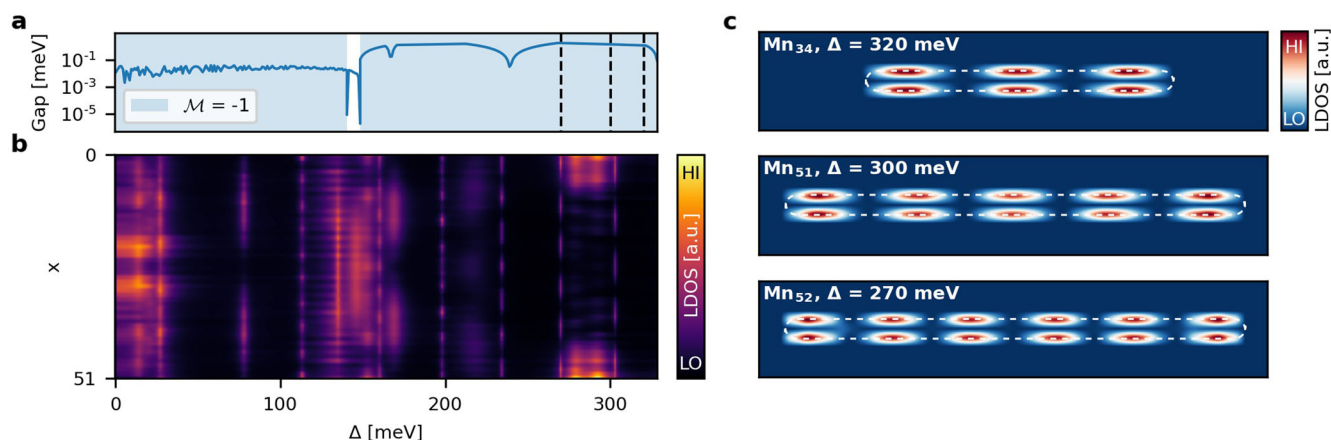
Fig. 2 Analysis of DFT-based superconducting 80-band model. a Topological phase diagram as a function of the bare superconducting amplitude Δ (topological region in blue with $\mathcal{M} = -1$, and white is trivial). The gap size is shown as the blue curve. **b** Zero-energy LDOS as a function of lattice site along x and Δ (the y-dependence has been summed up such that the LDOS appears one-dimensional) for chain length $N = 51$. **c** Examples of zero-energy LDOS(x, y) for various values of Δ, as indicated by the dashed vertical lines in (**a**), with pronounced side features. Chain length and Δ are given within the panels. The theoretical LDOS is always evaluated in the plane of the chain (for a discussion of the three-dimensional LDOS see Supplementary Note 4).

a striking similarity to recently reported scanning tunneling spectroscopy (STS) measurements on a Mn_{34} chain on Nb(110)[20] (i.e., a chain consisting of 34 Mn atoms). We show in Fig. 2c three examples of the zero-energy LDOS corresponding to different values of Δ and different chain lengths: a Mn_{34} chain with $\Delta = 320$ meV (three maxima), a Mn_{51} chain with $\Delta = 300$ meV (five maxima) and a Mn_{52} chain with $\Delta = 270$ meV (six maxima). Their topological gap sizes for open boundary conditions are 3.10, 1.37, and 0.88 meV, respectively. We note that a self-consistent treatment will typically suppress Δ near the magnetic chain, reducing the effective gap by a sizeable amount. This reduction can easily be as large as a factor of 3 or 4, which would bring the theoretical gap size to the same range as the experimental gap size of 180 μeV of one of the multi-orbital YSR-bands in the vicinity of the Mn[001] chains on Nb(110)[20] (which is a factor of 8 smaller than the superconducting bulk gap, $\Delta_{Nb} = 1.51$ meV). We emphasize that localization is governed by the coherence length, and thus longer chains lead to stronger localization of MZMs at the chain ends (see Supplementary Note 3.D). We note that side features can be observed for several values of Δ per chain length; we further note that MZMs can also appear in the chain center or combinations of side and center atoms (see for instance Supplementary Fig. 3). It turns out that contributions from different orbitals are sensitive to the chosen value of Δ, leading to a complex, non-trivial interplay of the five d-orbitals in the low-energy LDOS. All theoretical LDOS plots shown in the main text are purely two-dimensional. In the Supplementary Note 4, we extend our analysis by including tip trajectory and tunneling geometry and show that the 3D LDOS still contains sides features; all our conclusions remain, hence, unchanged.

Throughout the manuscript, we use the term MZM for the low-energy or zero-energy states of the topological superconducting phase. The latter is determined by the topological invariant for both infinite and finite chains. Clearly, several of the considered examples of MZM are (strongly) hybridized, and in the literature alternative names such as 'precursor of MZMs' have been introduced[31]. It is unknown whether hybridized MZMs are useful for braiding and thus for topological quantum computing, but that is not the topic of our paper. The aim of this paper is to demonstrate that a DFT-based modeling leads to a topological superconductor with low-energy states which are exceedingly similar to what has been observed in the experiments.

Majorana zero modes with side features

In order to deepen our understanding of the side features in the zero-energy LDOS, we analyze in the following a simplified model. Inspired by relevant orbitals of the 80-band DFT-based model which lead to side features, we construct a one-orbital model which still has three "substrate" atoms carrying superconductivity and one magnetic atom (modeled by a Zeeman term), see Fig. 3a. We stress that the model still contains a non-trivial hopping structure which could not have been guessed by an ad hoc toy model; the multi-band DFT input is key to derive and justify this 'simplified' model. We find for large gaps localized MZMs in the center of the chain ends (either on the magnetic or on the substrate atom), in agreement with previous modeling. However, when reducing the gap size (in an attempt to simulate the small experimental gap size), we find that the spectral weight of the MZMs drops to almost zero on the magnetic atoms. Moreover, spectral weight appears on the side-Nb atoms, in agreement with the DFT-based model, reminiscent of previous experimental findings[20]. A logical explanation for the formation of side features is as follows: the gap size corresponds to the strength of the superconductivity and thus to the proximity effect. In case of a large gap, i.e., of a significant superconducting proximity effect, superconductivity can be induced into the magnetic atoms and the MZM can be localized on the magnetic atoms at the chain ends. If the gap is small, however, the proximity-induced superconductivity competes with the magnetism of the Mn atoms, leading to suppressed superconducting correlations, and the MZMs are pushed away and localize along both sides instead.

The simplified model allows us to tune various parameters such as Rashba spin–orbit coupling, magnetic moment, chemical potential and superconducting pairing amplitude. We have analyzed the corresponding phase diagram and computed the fraction of the zero-energy LDOS which is localized on the side next to the magnetic chain. 40 percent of the topological region of the phase diagram Fig. 3c turns out to exhibit notable side features, and ten percent of the examined parameter space possess 70–99 percent of the total spectral weight on the sides of the chain. We have also analyzed a variant of the model with an extended substrate in both x- and y- direction to rule out confinement effects perpendicular to the chain. We find that side features persist regardless of the size of the substrate or its boundary conditions (see Supplementary Note 3.F for details). These findings emphasize that side features in the low-energy LDOS are not the exception but can be rather common. The
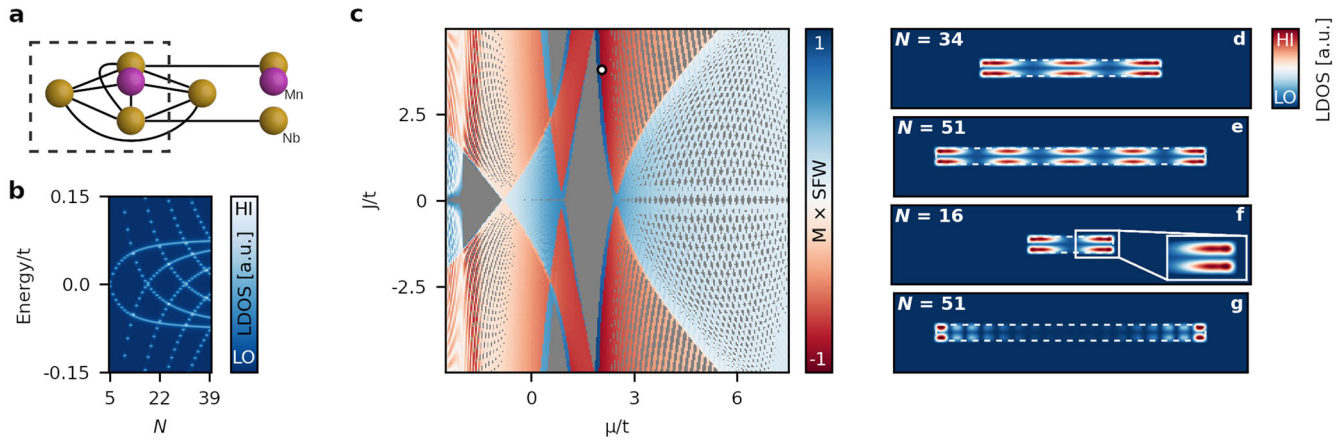
Fig. 3 Properties of simplified model for Majorana modes with side features. a Definition of unit cell and hoppings of the simplified model. **b** Evolution of the side features with chain length N in analogy to the experimental Fig. 4b. Parameters: $(\Delta, a, \mu, J) = (0.05, 0.01, 2.05, 3.4)t$. **c** Representative topological phase diagram for $\Delta = 0.05t$, $a = 0.01t$ and $N = 51$. Topologically non-trivial (trivial) regions are shown in red (blue), and are multiplied with the *side feature weight* (SFW) which quantifies how much spectral weight is accumulated on the side-Nb atoms (see Supplementary Note 3.B for details). Gray regions correspond to lowest energy states with $E > 0.04t$, which are thus not of interest. The white dot marks the parametric location of Fig. 1e. **d** Real-space zero-energy LDOS(x, y) with side features revealing a periodic pattern reminiscent of a Mn_{34} chain on Nb(110)[20]. Parameters: $(\Delta, a, \mu, J) = (0.05, 0.01, 2.05, 3.4)t$. **e** Real-space zero-energy LDOS(x, y) with side features revealing a periodic pattern reminiscent of a Mn_{51} and Mn_{52} chains on Nb(110), *c.f.* Fig. 4a. Parameters: $(\Delta, a, \mu, J) = (0.05, 0.01, 2.05, 3.8)t$. **f** Real-space zero-energy LDOS(x, y) with side features with reduced periodic pattern in the bulk reminiscent of a Fe_{16} chain on Nb(110), *c.f.* Fig. 4c. Parameters: $(\Delta, a, \mu, J) = (0.1, 0.05, 2, 4.9)t$. **g** Real-space zero-energy LDOS(x, y) with side feature only at the chain ends, reminiscent of the observed double-eye feature for Fe chains on Pb(110)[24]. Parameters: $(\Delta, a, \mu, J) = (0.15, 0.1, 1.35, 6)t$. The zero-energy LDOS states shown in **d–g** are in the topological phase.

oscillating behavior of the low-energy modes is a more ordinary hybridization effect, which has previously been discussed in the context of other systems[3,30,33–35]. We find that the smallest considered gap sizes lead to an equally-distributed pattern of oscillatory maxima along the chain (Fig. 3e, as found for the Mn_{51} chain in Fig. 2c). We also computed the evolution of side-feature states with chain length N displaying an oscillatory behavior of the low-energy states, see Fig. 3b.

When we slightly increase the gap size, these maxima disappear in the middle of the chain, but persist closer to the chain ends (an example with two such maxima at the chain ends is shown in Fig. 3f). Finally, we also find situations where MZMs are confined to the ends of the chains, still showing the side feature (Fig. 3g). We obtain a clear physical picture which emerges from our analysis: (i) when the substrate is included (via the three extra atoms per unit cell) and the gap is small, MZMs are forced to localize beside the magnetic chain on the substrate; (ii) for the smallest gap sizes considered, hybridization of MZMs is so strong that we obtain a periodic pattern of maxima in the zero-energy LDOS [see Fig. 3d and e], as previously observed for the ab initio computed Mn_{51} chain in Fig. 2c and for a measured Mn_{34} chain in ref. [20]. This is in agreement with a very large coherence length $\xi \sim v_F/\Delta_{gap}$ exceeding the chain length (see Supplementary Note 3.D). Increasing the gap size reduces ξ and leads to a decaying envelope of the wavefunction, such that spectral weight in the bulk of the chain is suppressed.

Larger gap sizes result in even stronger localization of the MZMs (see Fig. 3g), showing a remarkable similarity to what was observed for an Fe chain on a Pb(110) substrate[24]. We have computed coherence lengths and low-energy LDOS for small, medium, and large gap sizes for extended parameter ranges, all in support of our previous conclusions (see Supplementary Notes 3.C and 3.D). While our ab initio model does not describe the Fe/Pb(110) system, we can still speculate that the topological low-energy features might not depend on the specific system: there is clearly a strong similarity of the observed side feature with shorter coherence length (Fig. 3g) and the "double eye" seen in experiments[24]. Due to the topological character we propose that

the double eye feature found in Fe/Pb(110) has the same origin as the side features reported and modeled in this paper.

Experiment

To test the theoretical findings presented above, we studied linear chains of Mn and Fe assembled via lateral atom manipulation techniques on a clean Nb(110) surface[20,31,36] (see refs. [20,31] and Supplementary Note 5 for details on sample preparation and chain construction). Figure 4a shows the topography of a Mn_{51} chain assembled along the [001] direction (upper panel), together with the spatial form of dI/dV for a state close to zero energy. The side features visible in dI/dV exhibit a close spatial similarity with those that exist in the theoretical LDOS shown in Figs. 2c and 3e (previously reported side features, such as those shown in Fig. 3 of ref. [20], also exhibit a close similarity with Figs. 2c and 3d). The energy at which these side features are visible varies with the chain length N[20]; the evolution of the side features' energies with N is shown in Fig. 4b. Notably, the lowest energy state exhibiting these side features does not converge to $E = 0$ for chain lengths up to $N = 36$ but rather oscillates around zero energy. This result resembles the theoretical predictions shown in Fig. 3b (see also Supplementary Note 3.E) for a system with a small super-conducting gap, and a chain length that is smaller than the coherence length. The combination of these two renders the experimental resolution of a topological gap exceedingly difficult. Indeed, our numerical simulations show that for the case shown in Fig. 3b, the chain length has to be significantly larger before a topological gap can be resolved and the Majorana mode is clearly separated from the bulk states.

To study the universality of the observed side features, we also investigated the low-energy properties of a Fe_{16} chain along the [001] direction. This chain is structurally identical (see upper panel in Fig. 4c) to the Mn chains presented in Fig. 4a and ref. [20], and predicted to have a ferromagnetic ground state as well[26]. It also exhibits an enhanced zero energy dI/dV at both sides of the chain ends (lower panel in Fig. 4c). The notable similarity of these results with the theoretical calculations presented in Fig. 3f suggests a
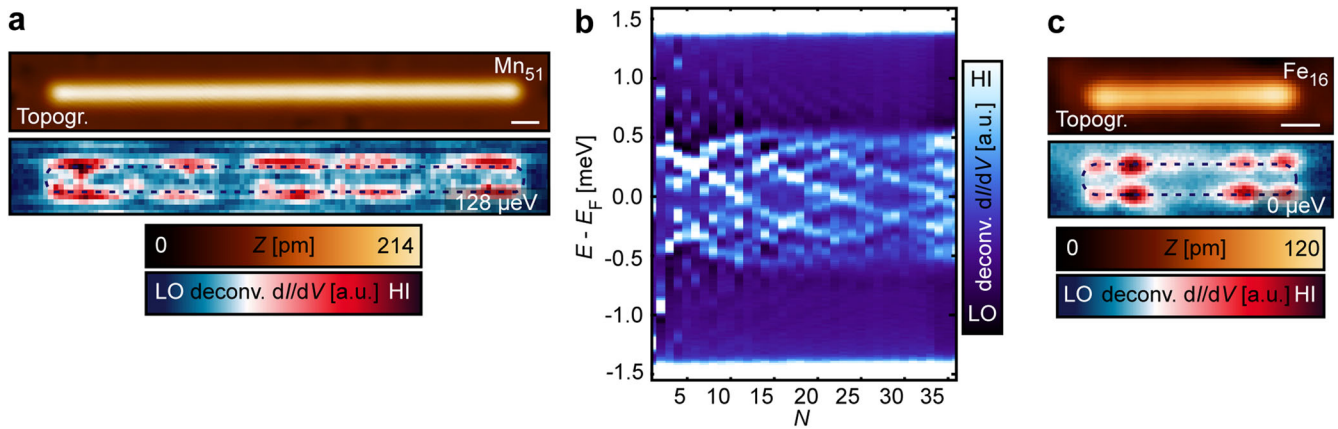
Fig. 4 Experimental observation of low-energy side features in linear atomic Mn and Fe chains on Nb(110). a Constant-current image (top panel) and deconvoluted dI/dV map (bottom panel) at $E = 128\,\mu\text{eV}$ for a Mn_{51} chain along the [001] direction. The white bar corresponds to 1 nm. The apparent extent of the chain from the upper panel is marked by the dark dashed lines in the dI/dV map. **b** Deconvoluted dI/dV spectra measured on the side of Mn_N chains' one end while additional Mn atoms were attached to the chain on the other end, thereby mainly showing the evolution of the side features with chain length N (c. f. refs. [20,31]). **c** Constant-current image (top panel) and deconvoluted dI/dV map (bottom panel) at zero energy for a Fe_{16} chain along the [001] direction, which is structurally identical to the Mn chain in panel (**a**). The white bar corresponds to 1 nm. The apparent extent of the chain from the upper panel is marked by the dark dashed lines in the dI/dV maps. Parameters: $V_{\text{stab}} = -6\,\text{mV}$, $I_{\text{stab}} = 1\,\text{nA}$, $V_{\text{mod}} = 20\,\mu\text{V}$.

common origin of the side features observed for the Mn_{51} and Fe_{16} chains on Nb(110).

DISCUSSION

The side features of the Mn chains were previously ascribed to bands formed by hybridization of Yu–Shiba–Rusinov (YSR) states of particular orbital character of the individual Mn impurities[20,37]. Individual Fe atoms do not exhibit clear signatures of multi-orbital YSR states[38,39] (see Supplementary Note 6 for details), due to their close proximity to the coherence peaks of the substrate. Nevertheless, the linear Fe chains along the [001] direction, mentioned above, show an enhanced zero-energy LDOS at the sides of both ends (Fig. 4c). This surprising observation, which cannot be explained by a linear combination of YSR states of the individual atoms (see Supplementary Note 6), shows obvious similarities with the theoretical calculations presented in Figs. 2c and 3. The interpretation of the observed side features as hybridized Majorana modes, as advocated in the theoretical part of this paper, is thus substantiated by the attempt to simultaneously explain the low-energy features for Mn and Fe chains on Nb(110).

Motivated by our analysis relating these findings with the previously discovered double-eye feature[24], we thus conclude that MZMs with side features might be a common phenomenon in MSH materials with small superconducting gap size. We note, however, counter examples do exist such as Fe/Re(0001)[18,19] and Mn chains along [1$\bar{1}$0] on Nb(110)[31]. This is, in fact consistent with our analysis of the superconducting 80-band model: side features appear only for certain values of Δ, and changing Δ leads to a redistribution of the relative orbital weight. Since some of the Mn d-orbitals support side features and others do not (see discussion of Supplementary Fig. 3), these 'counter examples' are compatible with the main results of our work. We emphasize that our results have far-reaching consequences: the presence of point-like zero-energy modes at chain ends is considered as a necessary condition for the identification of one-dimensional topological superconductors. Our work suggests that MZMs could, in fact, come in a large variety, ranging from delocalized, hybridized MZMs along the chain to localized MZMs on the chain. What determines whether a system is topological or not is not the spatial form of the lowest energy state, but the calculated value of the topological invariant. Our findings raise the important question whether MZMs with side features can be used for

braiding and topological quantum computing, emphasizing the necessity to perform further theoretical and experimental work on one-dimensional MSH structures.

METHODS

Density functional theory calculations

We are using fully relativistic all electron DFT calculations based on the full potential local orbital (FPLO) basis[40] in combination with a generalized gradient approximation (GGA) to the exchange correlation functional. We obtain low energy tight binding models using projective Wannier functions[27]. The considered slab super-cell is shown in Fig. 1a. We have fully relaxed the top half of the system while keeping the two bottom layers fixed at the Nb bulk lattice parameters and internal coordinates in order to simulate the experimental Nb(110) surface. We find that the top Nb layers contract slightly, lowering the nearest neighbor bond lengths. High symmetry positions for the placement of Mn are on top of Nb atoms and in the central hollow of the diamond arrangement of four Nb surface atoms. Energetically, the hollow position is 1.4 eV/Mn more favorable, in agreement with experimental observations and the calculations in ref. [37]. The Nb atoms forming bonds with Mn are measurably distorted out of their equilibrium Nb surface positions.

Superconducting 80-band modeling

The projected 40-band tight-binding model is given by

$$H = \sum_{i,j;o,o';\sigma,\sigma'} t^{i,o;j,o'}_{\sigma\sigma'} c^{\dagger}_{i,o,\sigma} c_{j,o',\sigma'} + \text{H.c.} \tag{1}$$

including essentially all possible hopping combinations up to fifth neighbors. Hopping amplitudes $t^{i,o;j,o'}_{\sigma\sigma'}$ are given as an input from DFT, and $c^{\dagger}_{i,o,\sigma}$ creates an electron with spin σ at orbital o at site i. We add the superconducting onsite pairing term $H_\Delta = \sum_{i,o} \Delta c^{\dagger}_{i,o,\uparrow} c^{\dagger}_{i,o,\downarrow} + \text{H.c.}$ and convert the model into an 80-band Bogoliubov-de Gennes model. As stressed before, the orbital index o only runs over the orbitals of the Nb atoms. We have calculated the topological invariant[1] both in momentum and real space[32] for this model. By virtue of Fourier transformation, we obtained the real-space representation, leading to matrix dimensions of $80N$ for chain length N, which can be diagonalized numerically. Open boundary conditions are enforced by setting all

hopping amplitudes connecting the two chain ends to zero; to make the chain mirror symmetric, the central Nb atom is removed on the left side of the chain. In the Supplementary Note 3.F, we investigate finite chains embedded in a larger substrate in order to rule out edge and confinement effects.

Scanning tunneling microscopy and spectroscopy

The STM experiments were performed in a home-built UHV facility operated at a base temperature of $T = 320$ mK[41]. The Nb(110) single crystal substrate was cleaned by high temperature flashes to $T > 2700$ K, following ref. [42]. Single Mn and Fe atoms were deposited onto the cold sample surface held at $T < 7$ K. A superconducting tip was prepared by indenting an electrochemically etched W tip into the substrate, thereby transferring large clusters of superconducting Nb onto the tip apex. STM topography images were measured in a constant-current mode with the current setpoint I while applying a constant bias voltage V_{DC} across the tunneling junction. Differential tunneling conductance (dI/dV) spectra were measured by stabilizing the tip at bias voltage V_{stab} and current I_{stab}. In the next step, the feedback loop was opened and V_{DC} was swept between -4 and $+4$ mV. The dI/dV signal was measured using a standard lock-in technique with a small modulation voltage V_{mod} (RMS) of modulation frequency $f = 4.142$ kHz added to V_{DC}. The dI/dV maps were acquired by recording a set of dI/dV spectra on a rectangular grid. Superconducting Nb tips have been used in order to achieve a higher effective energy resolution. The measured differential tunneling conductance dI/dV is thus approximately proportional to a convolution of the LDOS of the sample and the superconducting tip density of states (DOS). We show numerically deconvoluted STS data throughout the manuscript, resembling the sample's LDOS (see refs. [20,31] for details on the deconvolution process and determination of the tip gap). The Mn and Fe chains were assembled using lateral atom manipulation[18,36,43] techniques at low tunneling resistances of $R \approx 12$–60 kΩ.

DATA AVAILABILITY

REFERENCES

1. Kitaev, A. Y. Unpaired Majorana fermions in quantum wires. *Phys.-Usp.* **44**, 131–136 (2001).
2. Mourik, V. et al. Signatures of Majorana fermions in hybrid superconductor-semiconductor nanowire devices. *Science* **336**, 1003–1007 (2012).
3. Albrecht, S. M. et al. Exponential protection of zero modes in Majorana islands. *Nature* **531**, 206–209 (2016).
4. Deng, M. T. et al. Anomalous zero-bias conductance peak in a Nb-InSb nanowire-Nb hybrid device. *Nano Lett.* **12**, 6414–6419 (2012).
5. Ivanov, D. A. Non-Abelian statistics of half-quantum vortices in *p*-wave superconductors. *Phys. Rev. Lett.* **86**, 268–271 (2001).
6. Nayak, C., Simon, S. H., Stern, A., Freedman, M. & Das Sarma, S. Non-Abelian anyons and topological quantum computation. *Rev. Mod. Phys.* **80**, 1083–1159 (2008).
7. Pientka, F., Glazman, L. I. & von Oppen, F. Topological superconducting phase in helical Shiba chains. *Phys. Rev. B* **88**, 155420 (2013).
8. Li, J. et al. Topological superconductivity induced by ferromagnetic metal chains. *Phys. Rev. B* **90**, 235433 (2014).
9. Nadj-Perge, S., Drozdov, I. K., Bernevig, B. A. & Yazdani, A. Proposal for realizing Majorana fermions in chains of magnetic atoms on a superconductor. *Phys. Rev. B* **88**, 020407 (2013).
10. Schecter, M., Flensberg, K., Christensen, M. H., Andersen, B. M. & Paaske, J. Self-organized topological superconductivity in a Yu–Shiba–Rusinov chain. *Phys. Rev. B* **93**, 140503 (2016).
11. Klinovaja, J., Stano, P., Yazdani, A. & Loss, D. Topological superconductivity and Majorana fermions in RKKY systems. *Phys. Rev. Lett.* **111**, 186805 (2013).
12. Martin, I. & Morpurgo, A. F. Majorana fermions in superconducting helical magnets. *Phys. Rev. B* **85**, 144505 (2012).
13. Nadj-Perge, S. et al. Observation of Majorana fermions in ferromagnetic atomic chains on a superconductor. *Science* **346**, 602–607 (2014).
14. Ruby, M. et al. End states and subgap structure in proximity-coupled chains of magnetic adatoms. *Phys. Rev. Lett.* **115**, 197204 (2015).
15. Pawlak, R. et al. Probing atomic structure and Majorana wavefunctions in mono-atomic Fe chains on superconducting Pb surface. *npj Quantum Inf.* **2**, 16035 (2016).
16. Jeon, S. et al. Distinguishing a Majorana zero mode using spin-resolved measurements. *Science* **358**, 772–776 (2017).
17. Ruby, M., Heinrich, B. W., Peng, Y., von Oppen, F. & Franke, K. J. Exploring a proximity-coupled Co chain on Pb(110) as a possible Majorana platform. *Nano Lett.* **17**, 4473–4477 (2017).
18. Kim, H. et al. Toward tailoring Majorana bound states in artificially constructed magnetic atom chains on elemental superconductors. *Sci. Adv.* **4**, eaar5251 (2018).
19. Schneider, L. et al. Controlling in-gap end states by linking nonmagnetic atoms and artificially-constructed spin chains on superconductors. *Nat. Commun.* **11**, 4707 (2020).
20. Schneider, L. et al. Topological Shiba bands in artificial spin chains on superconductors. *Nat. Phys.* **17**, 943–948 (2021).
21. Choy, T.-P., Edge, J. M., Akhmerov, A. R. & Beenakker, C. W. J. Majorana fermions emerging from magnetic nanoparticles on a superconductor without spin–orbit coupling. *Phys. Rev. B* **84**, 195442 (2011).
22. Crawford, D., Mascot, E., Morr, D. K. & Rachel, S. High-temperature Majorana fermions in magnet-superconductor hybrid systems. *Phys. Rev. B* **101**, 174510 (2020).
23. Mier, C., Choi, D.-J. & Lorente, N. Calculations of in-gap states of ferromagnetic spin chains on *s*-wave wide-band superconductors. *Phys. Rev. B* **104**, 245415 (2021).
24. Feldman, B. E. et al. High-resolution studies of the Majorana atomic chain platform. *Nat. Phys.* **13**, 286–291 (2017).
25. Kobiałka, A., Piekarz, P., Oleś, A. M. & Ptok, A. First-principles study of the non-trivial topological phase in chains of 3*d* transition metals. *Phys. Rev. B* **101**, 205143 (2020).
26. Laszloffy, A., Palotas, K., Rozsa, L. & Szunyogh, L. Electronic and magnetic properties of building blocks of Mn and Fe atomic chains on Nb(110). *Nanomaterials* **11**, 1933 (2021).
27. Eschrig, H. & Koepernik, K. Tight-binding models for the iron-based superconductors. *Phys. Rev. B* **80**, 104503 (2009).
28. Kitaev, A. Periodic table for topological insulators and superconductors. *AIP Conf. Proc.* **22**, 1134 (2009).
29. Schnyder, A. P., Ryu, S., Furusaki, A. & Ludwig, A. W. W. Classification of topological insulators and superconductors in three spatial dimensions. *Phys. Rev. B* **78**, 195125 (2008).
30. Stanescu, T. D., Lutchyn, R. M. & Sarma, S. D. Dimensional crossover in spin–orbit-coupled semiconductor nanowires with induced superconducting pairing. *Phys. Rev. B* **87**, 094518 (2013).
31. Schneider, L. et al. Precursors of Majorana modes and their length-dependent energy oscillations probed at both ends of atomic Shiba chains. *Nat. Nanotechnol.* **17**, 384–389 (2022).
32. Budich, J. C. & Ardonne, E. Equivalent topological invariants for one-dimensional Majorana wires in symmetry class D. *Phys. Rev. B* **88**, 075419 (2013).
33. Klinovaja, J. & Loss, D. Composite Majorana fermion wave functions in nanowires. *Phys. Rev. B* **86**, 085408 (2012).
34. Deng, M. T. et al. Majorana bound state in a coupled quantum-dot hybrid-nanowire system. *Science* **354**, 1557–1562 (2016).
35. Deng, M. T. et al. Nonlocality of Majorana modes in hybrid nanowires. *Phys. Rev. B* **98**, 085125 (2018).
36. Schneider, L., Beck, P., Wiebe, J. & Wiesendanger, R. Atomic-scale spin-polarization maps using functionalized superconducting probes. *Sci. Adv.* **7**, eabd7302 (2021).
37. Beck, P. et al. Spin–orbit coupling induced splitting of Yu–Shiba–Rusinov states in antiferromagnetic dimers. *Nat. Commun.* **12**, 2040 (2021).
38. Odobesko, A. B. et al. Observation of tunable single-atom Yu–Shiba–Rusinov states. *Phys. Rev. B* **102**, 174504 (2020).
39. Küster, F. et al. Correlating Josephson supercurrents and Shiba states in quantum spins unconventionally coupled to superconductors. *Nat. Commun.* **12**, 1108 (2021).

40. Koepernik, K. & Eschrig, H. Full-potential nonorthogonal local-orbital minimum-basis band-structure scheme. *Phys. Rev. B* **59**, 1743–1757 (1999).

41. Wiebe, J. et al. A 300 mK ultra-high vacuum scanning tunneling microscope for spin-resolved spectroscopy at high energy resolution. *Rev. Sci. Instrum.* **75**, 4871–4879 (2004).

42. Odobesko, A. B. et al. Preparation and electronic properties of clean superconducting Nb(110) surfaces. *Phys. Rev. B* **99**, 115437 (2019).

43. Eigler, D. M. & Schweizer, E. K. Positioning single atoms with a scanning tunnelling microscope. *Nature* **344**, 524–526 (1990).

AUTHOR CONTRIBUTIONS

M.S. and H.O.J. performed the DFT calculations and derived the 40-band tight-binding model. D.C., E.M., D.K.M., and S.R. performed all other theoretical modeling. P.B., R.W., and J.W. conceived the experiments. P.B. performed the measurements and analyzed the experimental data together with J.W. S.R. wrote the manuscript, with contributions from all authors. All authors contributed to the discussions and to correcting the manuscript.

COMPETING INTERESTS

The authors declare no competing interests.

ADDITIONAL INFORMATION

Supplementary information The online version contains supplementary material available at https://doi.org/10.1038/s41535-022-00530-x.

Correspondence and requests for materials should be addressed to Stephan Rachel.

Reprints and permission information is available at http://www.nature.com/reprints

Publisher's note Springer Nature remains neutral with regard to jurisdictional claims in published maps and institutional affiliations.